Elucidating Sodium Ion Storage Mechanisms in Hard Carbon Anodes at the Electronic Level

Qingbing Xia, Cheng-Lin Ko, Emily R. Cooper, Qinfen Gu, Ruth Knibbe, and Jeffrey R. Harmer**

Sodium-ion batteries (SIBs) are a promising technology for advanced energy storage systems. Hard carbon (HC) is a commonly used SIB anode material; however, the Na ion storage mechanism in HC remains poorly understood and highly debated. Here, the paramagnetic species in HC during Na ion storage are systematically studied to elucidate the underlying mechanism at an electronic level using high-resolution electron paramagnetic resonance (EPR) spectroscopy, complemented by in situ Raman spectroscopy, in situ synchrotron X-ray diffraction, and density functional theory calculations. This investigation identifies and characterizes the coexistence of two distinct intercalation processes in HC: Na ion intercalation and Na^+-solvent co-intercalation, which are active across both the sloping and plateau voltage regions. Additionally, in the sloping region, Na ions are also stored at in-plane Stone-Wales defect sites, which transition into a quasi-metallic state and subsequently to metallic Na as Na ion intercalation progresses. This transformation is driven by charge redistribution within the graphene layers. These insights establish a direct paramagnetic-electronic structure-electrochemical property relationship in HC, providing new insights into the Na ion storage mechanism. Furthermore, this study highlights the unique capability of EPR spectroscopy in elucidating the charge storage mechanism in electrode materials.

1. Introduction

Lithium-ion batteries (LIBs) are the most widely used battery technology in the past decade due to their high energy and power density.[1] In recent years, the high price and availability of lithium resources have triggered intensive efforts to develop alternative battery technologies.[2] Sodium-ion batteries (SIBs) are an ideal technology beyond LIBs, particularly for stationary energy storage systems and short- to moderate-range electric vehicles, due to the widespread natural abundance and cost-effectiveness of sodium resources.[2a,3] The operation principle of SIBs is similar to that employed by LIBs.[4] However, the SIB electrode material requirements are different from those of LIBs. For example, graphite is a standard anode material for commercial LIBs but is unsuitable for SIBs due to the thermodynamic instability of binary sodium-graphite intercalation compounds.[5]

Hard carbon (HC) is considered the most promising anode material for SIBs because of its abundant availability, low redox potential, and high reversible capacities.[6] HC is a type of disordered carbon material composed of graphitic-like domains formed by curved and defective graphene sheets. Unlike crystalline graphite, these graphene layers are not perfectly aligned, resulting in a more disordered structure. The curved configuration of the graphene layers generates numerous pores that are randomly distributed throughout the material, contributing to the significant porosity of HC. These unique HC structural features have a pronounced influence on its voltage-capacity profile for Na ion storage, leading to two distinct voltage regions: a sloping region at a higher voltage (above 0.1 V vs Na/Na^+) and a plateau region at a lower voltage (below 0.1 V vs Na/Na^+). The Na ion storage mechanism in HC remains poorly understood and is still a subject of considerable debate. Dahn et al. proposed the "insertion-absorption" model, in which the sloping region results from Na ion intercalation into the graphitic-like domains, and the Na ion filling of the pores leads to the plateau region.[7] Contrarily, Cao et al. introduced an "adsorption-insertion" model, where the sloping region was attributed to Na ion adsorption on the surface, while the plateau region results from Na ion intercalating into graphitic-like domains.[8] Later, Bommier et al.

Q. Xia, C.-L. Ko, E. R. Cooper, R. Knibbe
School of Mechanical and Mining Engineering
The University of Queensland
St Lucia, Brisbane, QLD 4072, Australia
E-mail: ruth.knibbe@uq.edu.au

J. R. Harmer
Australian Institute for Bioengineering and Nanotechnology
The University of Queensland
St Lucia, Brisbane, QLD 4072, Australia
E-mail: jeffrey.harmer@cai.uq.edu.au

Q. Gu
Australian Synchrotron
Clayton, Melbourne, VIC 3168, Australia

The ORCID identification number(s) for the author(s) of this article can be found under https://doi.org/10.1002/adfm.202421976

DOI: 10.1002/adfm.202421976

further revealed that following the intercalation process, Na ions fill the pores by adsorbing onto their surface toward the end of the plateau region.[9]

The challenges in interpreting the Na ion storage process in HC arise primarily from limitations of characterization techniques in probing HC's complex structure. Conventional materials characterization methods, such as X-ray diffraction (XRD) and Raman, have significantly advanced in studying electrode materials with well-ordered crystalline structures. However, their ability to capture the intricate structural changes occurring during electrochemical processes in disordered materials like HC is often limited, particularly at high resolution. For example, current research predominantly relies on the lower angle shift of the (002) diffraction peak observed through XRD as an indicator of Na ion intercalation in HC.[9c–f,10] However, this shift is not consistently observed, with reports suggesting that the (002) peak remains unchanged during sodiation.[11] This inconsistency is likely due to HC's large and variable interlayer spacing and disordered graphene layer arrangement, which form a broad (002) peak. This broadness complicates the detection of subtle changes, making it challenging for XRD to serve as a very sensitive technique for conclusively studying Na ion intercalation.

Similarly, in situ Raman spectroscopy studies have linked shifts in the G band to Na ion intercalation into graphitic-like domains. However, interpreting these shifts is not straightforward, as both shifted and unshifted G band positions have been reported.[11d,12] Current research has not fully elucidated how the sodium species are stored in HC, particularly in distinguishing between Na ion intercalation and Na^+-solvent co-intercalation since both lead to the G band shift. Furthermore, quasi-metallic Na species have been observed during the storage of Na ions in HC;[13] however, the mechanisms governing their formation and transition remain unexplored. These limitations underscore the need for more effective characterization techniques to accurately analyze the various reaction processes in HC.

Electron paramagnetic resonance (EPR) spectroscopy is a magnetic resonance technique that is highly sensitive to the number and local environment of unpaired electron spins, which are often difficult to characterize using conventional methods.[14] EPR spectroscopy, through its ability to probe unpaired electron spins, offers unique insights into the electronic structure and electrochemical reactions of electrode materials.[15] Consequently, EPR spectroscopy is a highly promising analytical tool for unraveling the charge storage mechanisms in electrode materials.

Here, we employ high-resolution multi-frequency continuous wave (CW) and pulse EPR spectroscopy from room temperature to cryogenic conditions. This characterization is complemented by in situ Raman, in situ synchrotron XRD, and density functional theory (DFT) calculations to understand the dynamic transition of unpaired electron spins in HC during electrochemical reactions. This multi-technique approach unveils changes in the electronic structure, providing new insights into the Na ion storage behaviors in HC. Our study reveals that in HC (1) Na ion intercalation dominates the capacity contribution, starts in the sloping region and progresses until ≈0.01 V in the plateau region; (2) Substantial charge transfer between the intercalated Na ions and graphene layers establishes a favorable local charge environment to drive the transition of surface adsorbed Na ions (located at in-plane defect sites) from an ionic state to a quasi-metallic state, eventually culminating in a metallic state at voltages below 0.01 V in the plateau region; (3) Na^+-solvent co-intercalation occurs concurrently with other processes in both the sloping and plateau regions, further contributing to the overall Na ion storage mechanism in HC.

2. Results

This study uses glassy carbon type HC,[16] as a model electrode material. **Figure 1a** shows a high-resolution transmission electron microscopy (HRTEM) image of an HC slice prepared using a focused ion beam (FIB). It reveals that HC consists of randomly oriented, turbostratic graphene layers with noticeable curvature. The observed lattice fringes indicate an average stacking distance of ≈0.36 nm between graphene layers. These curved graphene layers enclose pores of varying sizes and irregular shapes (highlighted by orange circles), randomly distributed throughout the material. However, accurately determining the exact pore shapes and sizes remains challenging due to the low contrast of the carbon atoms in the HRTEM image. These typical microstructure features of the HC are illustrated in the insert in Figure 1a. The XRD pattern (Figure 1b) shows the lack of long-range crystalline order in HC, evidenced by two broad peaks at ~24 and ~43°. These peaks are analogous to the (002) and (101) planes typically observed in graphite.[17] Notably, HC exhibits a larger interlayer distance of 0.359 nm compared to graphite (0.335 nm).

The Raman spectra in Figure 1c reveal two primary Raman-active modes at ≈1351 and 1592 cm^{-1}, corresponding to the D and G bands, respectively. Additionally, a 2D band at ≈2700 cm^{-1} indicates the formation of localized, short range graphitic-like domains in HC, where the graphene layers or segments achieve a higher stack order, tending to graphite's coherent stacking order. Two additional Raman bands at 271.4 and 456.2 cm^{-1} are attributed to Stone-Wales defects, implying the presence of non-hexagonal rings, e.g., five/seven-membered carbon rings.[18] These defects are significant in the HC materials due to their association with the curvature-related structural features of graphene layers. The impact of Stone-Wales defects on the Na ion storage mechanism in HC has not been extensively explored in past studies, particularly regarding their role in Na intercalation and the formation of quasi-/metallic Na. Therefore, the glassy carbon type HC is an ideal model for this purpose as it predominantly exhibits Stone-Wales defects.

The Na ion storage properties of HC were studied using a three-electrode cell, where HC was used as the working electrode and Na metal as both the counter and reference electrodes. The three-electrode cell helps to mitigate polarization effects that can influence the electrochemical potential of the HC electrodes. The typical voltage-capacity profiles (Figure 1d) show the coexistence of a sloping region and a plateau region during discharge, consistent with previous reports on HC anodes. Notably, the plateau region accounts for the majority of the total discharge capacity, constituting 83% in the first cycle and increasing to 90% in the second cycle. Additionally, a significantly higher sloping capacity of 47.3 mAh g^{-1} is achieved in the first cycle, which decreases to 23 mAh g^{-1} in the second cycle. This irreversible capacity loss can primarily be attributed to the formation of solid-electrolyte interphase (SEI).

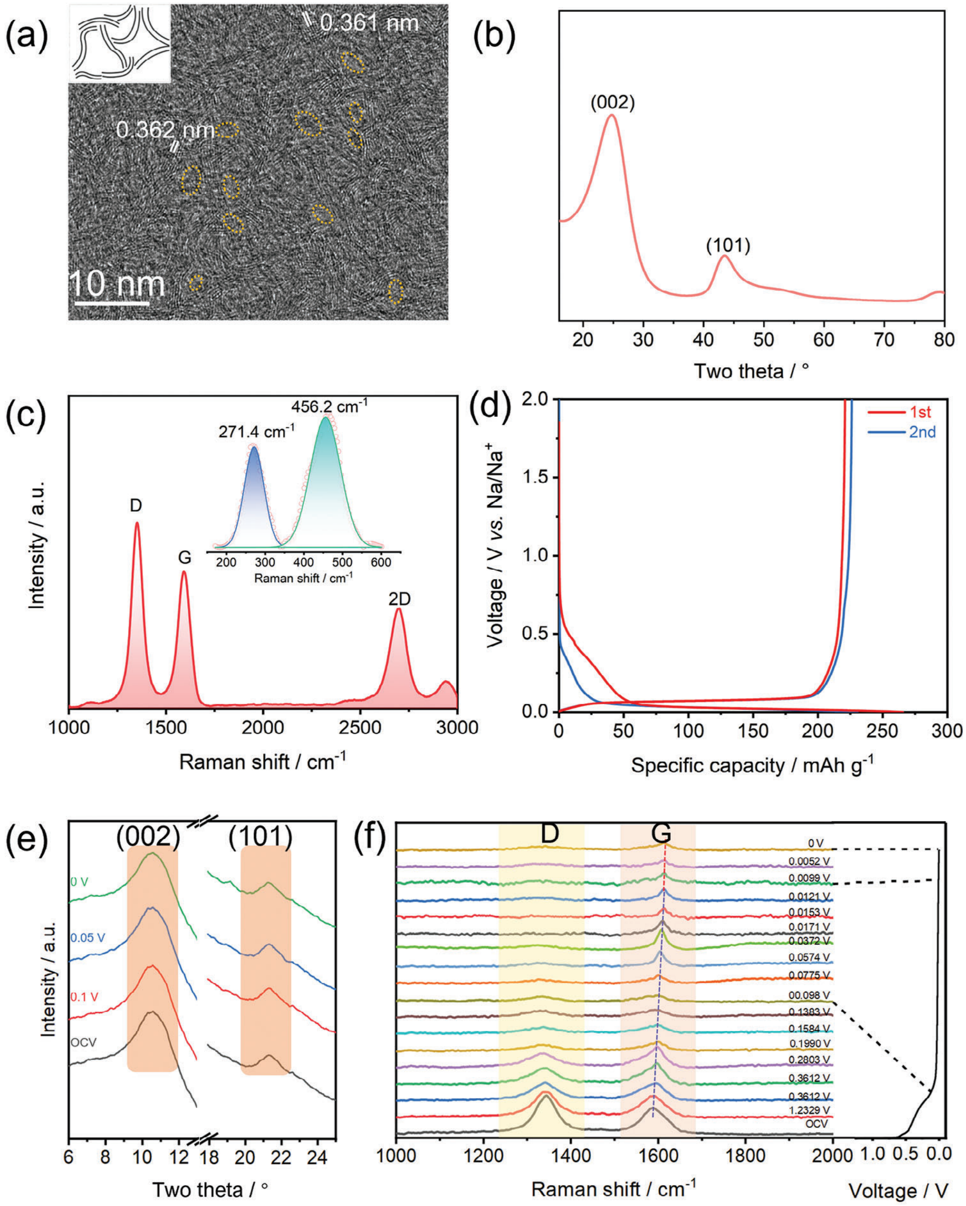

Figure 1. Structural and electrochemical characterisations of HC: a) HRTEM image. The insert illustrates the microstructure features. b) XRD pattern. The X-ray wavelength is 1.54184 Å. c) Raman spectra. Insert is the enlarged Raman spectrum between 150 and 600 cm^{-1}. d) Charge/discharge profiles at a current density of 10 mA g^{-1}. e) Synchrotron XRD patterns at different discharge states, with an X-ray wavelength of 0.68770 Å. f) In situ Rama spectra recorded during the discharge process.

To understand the Na ion storage mechanism in HC, we first studied the overall crystal structure variations of HC at different stage-of-discharge (SOD) (open-circuit [OCV], 0.1, 0.05, and 0 V) using synchrotron high energy XRD, as shown in Figure 1e. The analysis revealed that the characteristic diffraction peaks of (002) and (101) did not show significant changes in their *theta* positions. This lack of detectable change highlights the limitations of XRD in conclusively determining Na ion intercalation in HC.[9c–f,10,11] In situ Raman spectroscopy (Figure 1f) analysis was then conducted to study the Na ion storage process in HC. Unlike XRD, Raman spectroscopy offers more nuanced insights into the chemical structures and bonding environments of HC. The in situ Raman spectra reveal a significant reduction in the intensity of the D band during the sloping discharge process, indicating that Na ions are being adsorbed onto the Stone-Wales defect sites. Additionally, the G band shows a continuous blue shift and intensity fading throughout the sloping region and into the plateau region until the SOD of ≈0.01 V. The G band peak positions show a minor shift in the following discharge process. The G band frequency is highly sensitive to charge transfer between intercalated cations and graphene layers. The observed blue shift arises from increased force constants of the in-plane C—C bonds, driven by additional electrons introduced into the graphene layers.[19] These extra

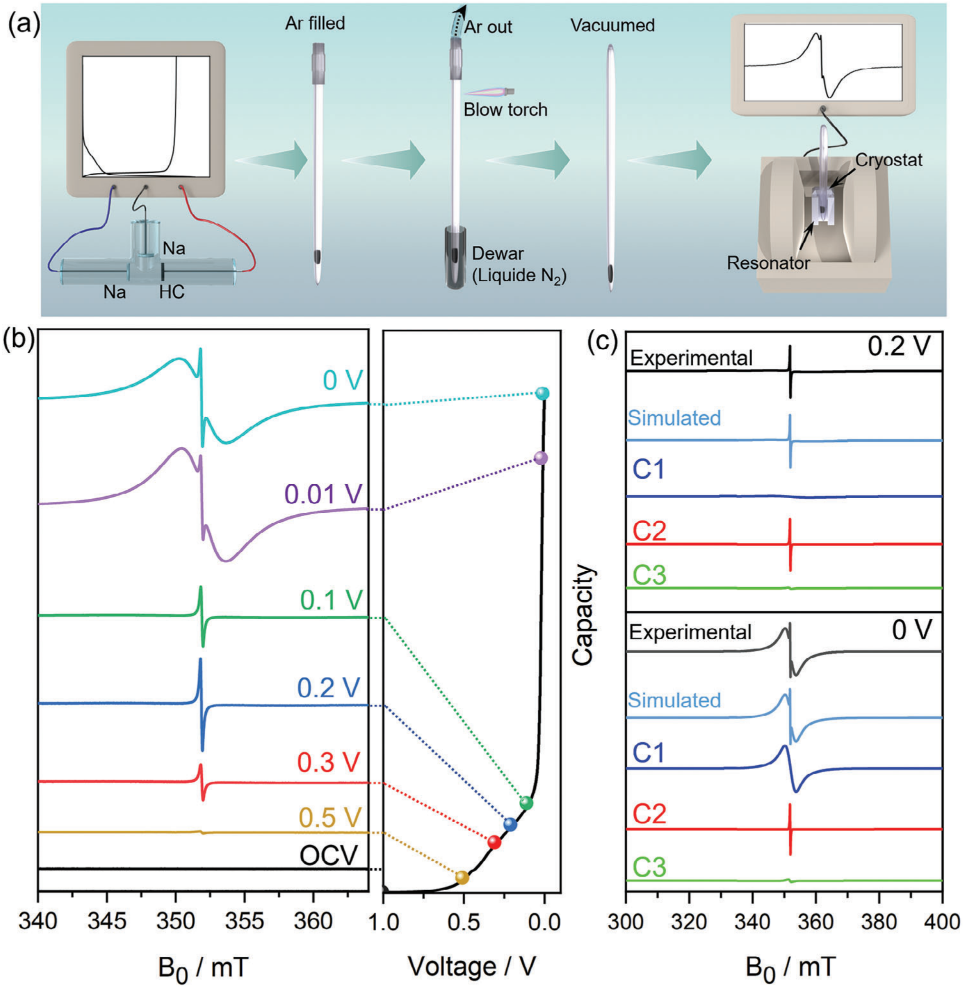

Figure 2. a) Schematic illustration of the experimental procedure for EPR characterisation. b) Room temperature X-band (9.8658 GHz) CW EPR spectra of HC at selected SODs, measured under non-saturating conditions and normalized by microwave power. The right panel shows the corresponding discharge profile. The EPR signal intensity has been normalized by the sample mass, and thus the signal intensity is proportional to the number of unpaired spins. c) Comparison of the EPR spectra at the SODs of 0.2 and 0 V.

electrons enhance electron-phonon coupling and strengthen bonding interactions within the graphene structure, altering the vibration modes of the carbon atoms.[20] The intensity fading of the G-band can be attributed to local electronic structure changes induced by the intercalation process. Specifically, during intercalation, electron redistribution occurs within the graphene layers, which alters the electronic environment of the carbon atoms. This redistribution weakens the overall Raman scattering cross-section, resulting in a decrease in the observed G-band intensity. The phenomenon of G band blue shift and intensity fading has also been observed during processes such as Li ion intercalation in graphite and pyrolytic graphite,[20a,21] Na$^+$-solvent co-intercalation in few-layered graphene[20b] and few-layer graphitic carbon,[22] as well as Na ion intercalation in aminobenzene functionalized graphene.[21] Therefore, while the in situ Raman results indicate the occurrence of an intercalation process in HC, they cannot directly distinguish whether this process arises from Na ion intercalation or Na$^+$-solvent co-intercalation.

To further understand the electrochemical process, high-resolution EPR spectroscopy was employed as illustrated in **Figure 2a**. Before EPR characterization, HC electrodes were discharged to the desirable SODs in three-electrode cells. After discharge, the HCs were collected, washed, vacuum-dried, and finally loaded into argon-filled thin-wall quartz tubes (3 mm diameter). These tubes were evacuated to a pressure of 1×10^{-4} Pa before being vacuum-sealed using a blowtorch. CW X-band EPR spectra of the HC at different SODs were recorded at room temperature, as plotted in Figure 2b and Figure S1 (Supporting Information).

The pristine HC electrode (at OCV) shows no distinguishable EPR signals, indicating the absence (or below the EPR detection limit) of mobile or localized unpaired electron spins.[14b] As the discharge progresses, a multi-component EPR signal is observed, suggesting the generation of dissociative unpaired electrons within the HC. To accurately model the spectra recorded at all SODs, three EPR components were required (Figure 2c; Figure S2, Supporting Information): a broad component (C1)

Table 1. EPR model parameters for C1, C2, and C3. The parameters include the number of spins per gram, mean *g*-value (*g*), and linewidth (*LW*, in mT).

SOD [V]	spins [$\times 10^{19}$ g^{-1}]				C1		C2		C3	
	total	*C1*	*C2*	*C3*	*g1*	*LW1*	*g2*	*LW2*	*g3*	*LW3*
0.5	0.1	0.1	<0.005	<0.005	2.010	34	2.003	0.45	2.004	1.7
0.3	3.0	3.0	<0.005	<0.005	2.005	28	2.003	0.27	2.004	1.7
0.2	3.5	3.4	0.023	0.02	2.004	21	2.003	0.24	2.004	1.7
0.1	5.7	5.6	0.018	0.01	2.005	26	2.003	0.24	2.004	1.7
0.01	15.6	15.5	0.025	0.04	2.002	6	2.003	0.24	2.004	1.7
0	17.2	17.1	0.027	0.07	2.003	6	2.003	0.22	2.004	1.7

that accounts for >97% of the total signal, and two narrow components (C2 and C3). The EPR fitting parameters are summarized in **Table 1**. During the sloping region, the EPR signal intensity is weak and comprises resonance lines centered around a *g*-value of 2, with both narrow and broad components present. However, it was difficult to separate the two narrower components C2 and C3 as they partially overlap and exhibited very weak signal intensity. In the plateau region the EPR signal intensity of C1 rapidly increases together with narrowing its linewidth. C1 shows the broadest linewidth, which decreases as the discharge progresses, particularly after 0.1 V where the number of unpaired electron spins increases very rapidly. This inverse correlation between linewidth and the number of spins is attributed to electron-electron exchange-narrowing interactions, which become more effective as the number of spins increases. Similar phenomena have also been observed in Li ion intercalation into graphite, where spin-orbit interactions between the σ-spin of the intercalated Li ions and the π-electrons in the graphene led to signal narrowing.[23] Accordingly, C1 is assigned to delocalized π-radicals generated during the intercalation process in the graphitic-like domains in HC.[14b,23a,b] Component C2 is centered at a *g*-value of 2.003 and is modelled with a narrow symmetric resonance line; its linewidth narrows slightly from 0.45 to 0.24 mT during the sloping region (until ≈0.2 V) and reaches its narrowest value of 0.22 mT (6.0 MHz) at 0 V. The third component, C3 has a *g*-value of 2.004 and a linewidth of 1.7 mT (48 MHz), both of which do not exhibit significant variations with the SODs.

To differentiate the origins of the three EPR components and their relationship to the Na ion storage process, temperature-dependent X-band CW EPR spectra were recorded across a temperature range from 295 to 5.4 K at selected potentials, as shown in **Figures** 3a, S3 and S4 (Supporting Information). Upon cooling the sample discharged to 0 V, the EPR signal intensities of C1 and C2 show only a very slight increase, whereas the intensity of C3 increases significantly (Figure 3b,c; Figure S5, Supporting Information). The slight intensity increase of C1 and C2 indicates electronic structures characteristic of a small band gap semiconductor or a metallic/semi-metallic species.[24] This observation supports the idea that C1 is attributed to the unpaired electron spins associated with sodiated HC, as the intercalation of cations between graphene layers modifies the electronic structure of HC, imparting paramagnetic species with metallic-like behavior to the material.[25] For C2, its low intensity increase indicates that it originates from a sub-/nano-scale Na species with quasi-/metallic electronic properties, considering its narrow and sharp symmetric resonance line. In stark contrast, the intensity of C3 exhibits a significant temperature dependent behavior, increasing by a large factor (>30) as the temperature is lowered from 295 to 5.4 K, and the temperature dependence of C3 aligns broadly with the expected response for an $S = ½$ electron spin governed by the Boltzmann distribution.[26] Such a response indicates that C3 arises from a localized radical that is relatively isolated and does not experience large electron-electron exchange interactions.

The interactions contributing to the EPR linewidths of three components were further investigated by a comparative study of the CW EPR spectra recorded at X-band (9.8658 GHz) and Q-band (34.00 GHz). The results in Figure 3d show that the linewidths of all three components remain essentially unchanged across both frequencies, indicating there is no appreciable broadening from anisotropy in the electron-Zeeman interactions (parameterized by *g*-values), which scale linearly with the magnetic field. For C1, this result supports the assignment of its broad width largely due to electron dipolar and exchange interactions, as well as lifetime broadening, which are consistent with an Na ion intercalation process. The characteristics of C2, which exhibits a homogeneously broadened line and averaged electron-Zeeman interactions due to itinerant electrons, further identifying it as being associated with quasi-/metallic Na species. C3, in contrast, describes localized paramagnetic centers associated with a carbon-based radical, which typically exhibit a small *g*-value anisotropy that is unresolved at Q-band frequencies due to the relatively broad spectrum width. This broadening is primarily governed by hyperfine interactions, which will be discussed in the following sections.

To further study the properties of the three EPR components, pulse measurements were carried out. Echo-detected field-swept EPR measurements were performed by recording the echo intensity from a primary echo sequence ($\pi/2 - \tau - \pi - \tau -$echo) as a function of the magnetic field B_0. As shown in Figure 3e, at the SOD of 0 V, neither C1 nor C2 produce an electron spin echo, whereas an echo was observed for C3. For C1, the lack of an echo is likely due to rapid spin relaxation, where the phase memory time (T_M) of the echo is shorter than the spectrometer deadtime (100 ns), preventing its detection. This interpretation aligns with the CW EPR data, where C1 remained unsaturated even under high microwave power irradiation at 5.4 K (Figure S6, Supporting Information). The absence of an electron spin echo for C2 indicates a homogenously broadened line caused by the averaging of

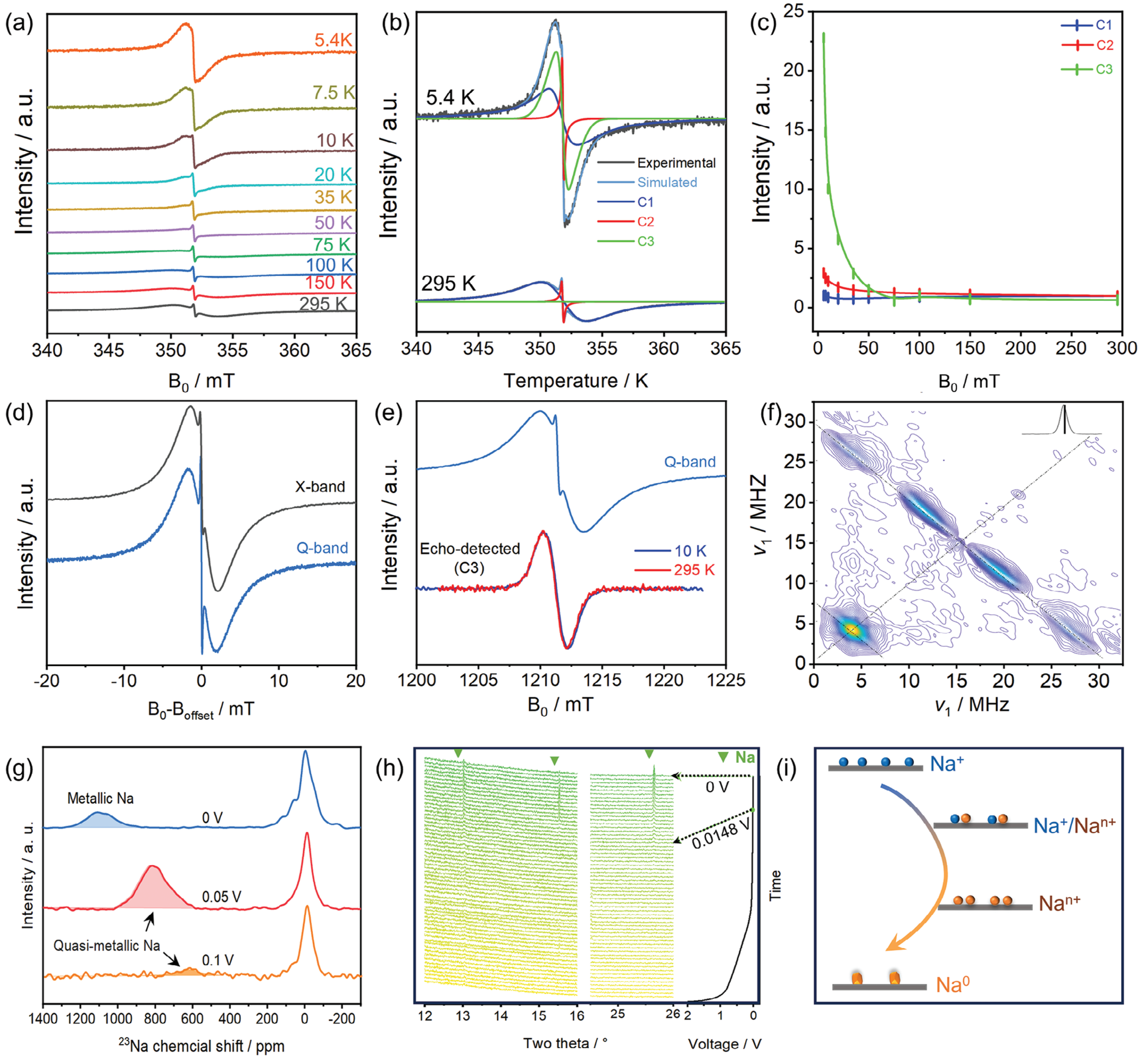

Figure 3. a) X-band CW EPR spectra of HC at a SOD of 0 V, recorded across a temperature range from 295 to 5.4 K. b) Simulated EPR spectra at selected temperatures of 295 and 5.4 K. c) Intensity verses temperature variation for C1, C2, and C3, derived from fits to the EPR spectra (Figure S5, Supporting Information). d) Room temperature X-band (9.8658 GHz) and Q-band (34.00 GHz) CW EPR spectra of HC at a SOD of 0 V. e) Q-band (34.00 GHz) CW EPR (295 K) spectrum and corresponding echo-detected field-swept spectra recorded at 295 K (red) and 10 K (blue). f) X-band (9.7835 GHz) HYSCORE spectra of HC at a SOD of 0 V. The insert shows the echo-detected field-swept spectrum and the horizontal line the experimental field position (348.8 mT). In the weak coupling case observed here, signal to 1st order is centered around the Larmor frequency ν (^{1}H: 14.9 MHz, ^{13}C: 3.7 MHz) and split by the corresponding hyperfine interaction A, e.g. for $\nu(^{1}\mathrm{H}) = 14.9 \pm A/2$ MHz. g) Ex situ ^{23}Na MAS NMR spectra of the HC at different SODs. h) In situ synchrotron XRD patterns of the HC during the discharge process. The sharp peaks refer to the diffraction peaks of metallic Na. The X-ray wavelength used was 0.6877 Å. i) Schematic illustration of the transition of Na species from ionic to quasi-metallic to metallic states.

interactions by itinerant electrons. This observation is consistent with the weak signal intensity increase with lower temperature, and indicates that the unpaired electron spins of C2 are associated with small quasi-metallic or metallic species. Conversely, the observation of an echo for C3 confirms its linewidth is inhomogeneously broadened, implying that the radical is localized and that its spectral width is largely due to magnetic interactions with neighboring magnetic nuclei. Additionally, the electron spin echo for C3 was also detected at the SODs of 0.3 and 0.2 V (Figures S7 and S8, Supporting Information).

C2 reveals the presence of quasi-/metallic Na species in HC during the discharge. However, due to their unique properties, these quasi-metallic Na species are inherently challenging to characterize.[13a,27] To further investigate their formation,

^{23}Na MAS NMR characterizations were carried out, as shown in Figure 3g. In the NMR spectra, a broad, high-intensity peak is characteristic of diamagnetic ionic sodium, originating from overlapping signals due to intercalated Na ions, residual electrolyte salts, Na-containing species in the SEI, and surface adsorbed Na ions.[9c,13b,27b] The presence of this broad peak provides evidence that Na ions are intercalated within the HC structure in an ionic state. However, due to the inherently disordered nature of HC, precise characterization of these intercalated compounds is challenging, as significant signal overlap obscures the specific contributions from different sodium species. At the SOD of 0.1 V, quasi-metallic Na clusters were detected, as evidenced by a broad peak corresponding to the ^{23}Na Knight shift between 500 and 700 ppm. This suggests the reduction of Na^+ to Na^{n+} ($0 < n < 1$) occurred. However, this peak shows a weak intensity due to the limited formation of quasi-metallic clusters at this stage. As the discharge progresses, this signal intensity increases and shifts to higher chemical shifts, reflecting an increased contribution from the Knight shift attributed to the enhanced Na 2s density of states at the Fermi level,[13a] with metallic Na being observed at a SOD of 0 V.

To understand the formation of metallic Na in HC, in situ synchrotron XRD analysis was carried out as shown in Figure 3h. Using high-energy X-rays with a wavelength of 0.6877 Å, shorter than conventional lab XRD at 1.54184 Å, synchrotron XRD provides a higher resolution for detecting structural information of the sodium species formed in the HC. Metallic Na was observed at a very low voltage below 0.0148 V. It is worth noting that this observation is crucial as it marks the first direct in situ detection of metallic Na formation in the HC anode during discharge. These results confirm the nature of C2 as a quasi-/metallic Na species. Therefore, there is an ionic to quasi-metallic to metallic transition of the Na species, as illustrated in Figure 3i. However, in the following charge process, it is found that the transition between ionic Na and metallic Na is only partially reversible, with some quasi-metallic Na persisting even after the full charge process (Figure S9, Supporting Information).

X-band hyperfine sublevel correlation spectroscopy (HYSCORE) was used to investigate electron-nuclear coupling to C3. The HYSCORE spectrum (Figure 3f) reveals that the paramagnetic center of C3 is coupled to nearby protons, with ^{1}H hyperfine couplings in the range $|A(^1H)| = 2$–28 MHz. Additionally, there is an intense signal at the ^{13}C Larmor frequency with small hyperfine couplings, approximately $|A(^{13}C)| \leq 1$ MHz, indicating C3 is also coupled to multiple carbon nuclei. These findings support the identification of C3 as a localized organic radical interacting with surrounding carbon atoms and protons, providing evidence for the occurrence of Na^+-solvent co-intercalation in HC, given that the primary source of ^{1}H nuclei in the system would be the solvent molecules (diglyme, $(CH_3OCH_2CH_2)_2O$). It is feasible that C3 may result from electrolyte decomposition or the SEI. To investigate these possibilities, we studied the electrolyte decomposition and detected no EPR signals (Figure S10, Supporting Information). Additionally, in the charged HC (charged to 3 V), only weak C3 signal was observed (Figure S9a,b, and Table S1, Supporting Information). Furthermore, the C3 signal does not increase in intensity in the prolonged cycled HC, despite the increased SEI formation. This suggests that C3 is unlikely to be from the SEI, as its intensity would be expected to increase along with SEI growth. Thus, C3 is interpreted as being associate with Na^+-solvent co-intercalation. It should be noted that the Na^+-solvent co-intercalation has been extensively studied in graphite anodes but has rarely been reported in HC anodes.[28]

Previous studies have shown that HC exhibits structural differences depending on its synthesis temperature,[29] which may potentially result in distinct Na ion storage mechanisms. Considering that the glassy carbon type HC used in the above experiments was synthesized at a high temperature above 2000 °C, we also conducted EPR analysis on HC synthesized at a lower temperature of 1000 °C, denoted as HC1000. The structural characterisations of HC1000 are detailed in Figure S11 (Supporting Information), and the EPR analysis is presented in Figure S12 (Supporting Information). At a SOD of 0 V, the room temperature EPR spectrum of HC1000 shows two visible components: a component with a linewidth of 12 mT, assigned to C1 (Na ion intercalation), and a second component with a linewidth of 0.55 mT. Upon cooling from 296 to 12 K, the EPR spectrum gradually converts into a single line with a width of 0.44 mT at 12 K. This behavior suggests that the narrow and broad EPR components observed at room temperature are electronically connected. As the temperature is lowered, increased conductivity enhances electron-electron exchange interactions between these components, leading to a single homogeneously broadened line. This effect makes it challenging to resolve a distinct metallic EPR signal at lower temperatures. Ex situ ^{23}Na MAS NMR characterization of the HC1000 reveals a quasi-metallic Na signal, supporting that Na ions undergo a transition to a quasi-metallic state. Although the results suggest the presence of C2 in HC1000, it remains difficult to precisely isolate this component in the EPR spectra, especially at low temperatures. Additionally, at low temperatures, a very weak electron spin echo was detected, allowing an EPR spectrum to be recorded that has position and linewidth characteristics of C3 in the above HC (glassy carbon type). This indicates a small population of isolated radicals, similar to what was observed in the HC (glassy carbon type), and is indicative of Na^+-solvent co-intercalation. However, the weak intensity of the signal prevented further analysis, such as obtaining proton coupling data from using HYSCORE. These findings collectively imply that Na ion intercalation, Na^+-solvent co-intercalation, and the transition from ionic to quasi-metallic Na states also occur in HC1000.

To investigate the impact of Na ion intercalation on the electronic structure and surrounding binding environment in HC, as well as its role in the Na evolution mechanism from ionic to quasi-metallic and metallic states, density functional theory (DFT) analysis was conducted. Structural models are shown in **Figure 4a**; pristine graphene (pG) and Stone-Wales defect graphene (dG) layers with Na adsorbed on the surface (Na_{ads}) and intercalated between the interlayer (Na_{inter}), as well as combinations of adsorption and intercalation (Na_{ads}-dG-Na_{inter}). The DFT results in Figure 4b show that dG exhibits a more negative binding energy (−7.921 eV) compared to pG (−7.696 eV) when interacting with Na, indicating that the Stone-Wales defects enhance the surface sodiophilicity, making it more attractive for Na adsorption. The strong interactions lead to the formation of Na_{ads}-C bonds with a bond length of 2.68 Å, comparable to bond lengths observed in organosodium molecules (2.5–3.2 Å).

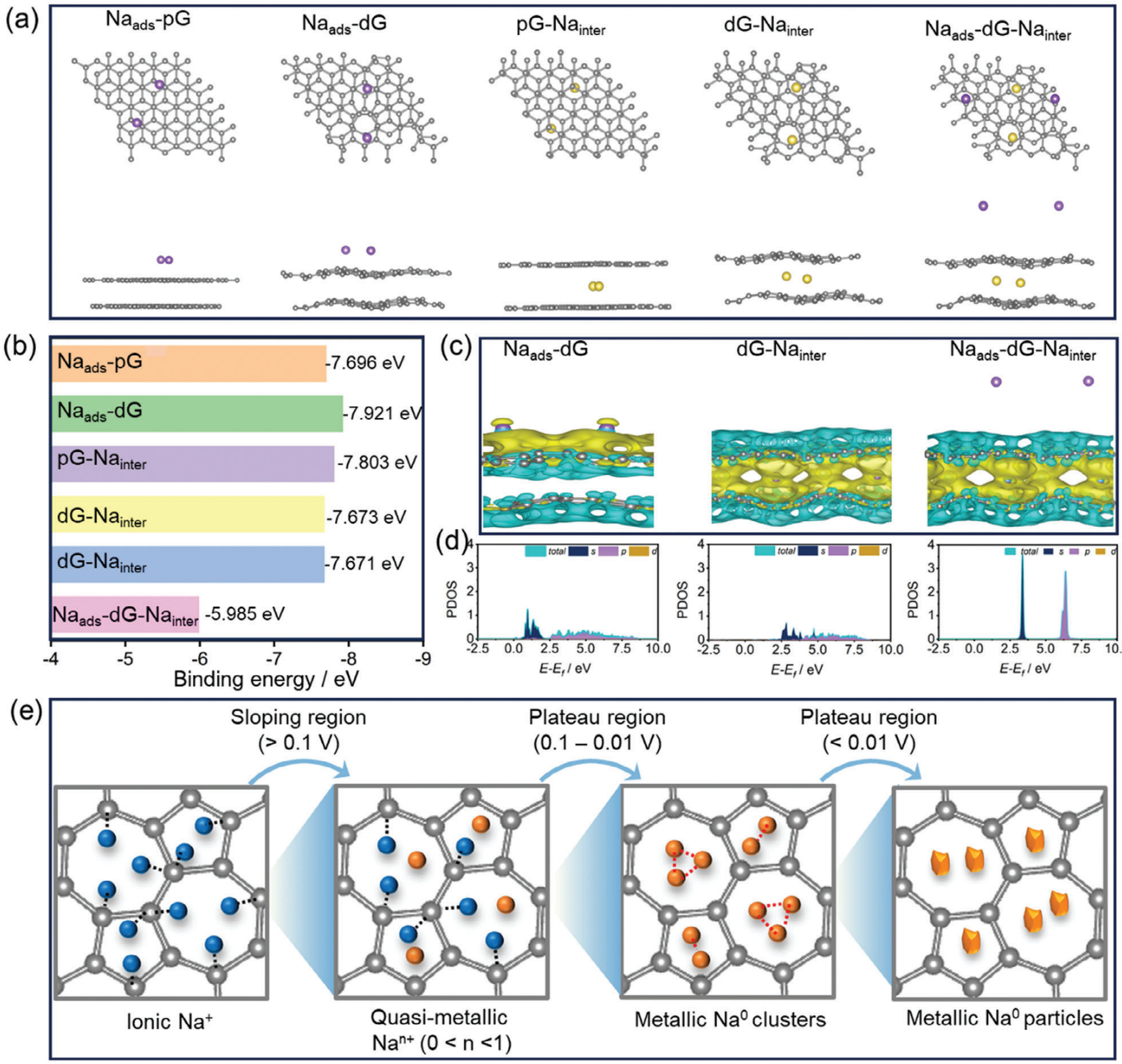

Figure 4. a) Projected structural models of the Na on (Na$_{ads}$) and intercalated (Na$_{inter}$) between planar pristine graphene (pG) and Stone-Wales defect graphene (dG) layers. b) Binding energy between Na and the graphene layers in different structural models. c) Isosurface of the charge density difference for Na$_{ads}$-dG, dG-Na$_{inter}$ and Na$_{ads}$-dG-Na$_{inter}$. The yellow and cyan surfaces represent the gain and loss of charge density, respectively. Na is represented by purple spheres. d) PDOS of Na$_{ads}$-dG, dG-Na$_{inter}$, and Na$_{ads}$-dG-Na$_{inter}$ models. e) Schematic illustration of the evolution of Na ions at the Stone-Wales defective sites.

However, dG exhibits weaker interaction with intercalated Na (Na$_{inter}$) between the interlayer, with a binding energy of −7.673 eV, compared to −7.803 eV for pG. Further calculations show that the pre-adsorption of Na$_{ads}$ on dG does not impact the binding of Na$_{inter}$ with the dG, as the binding energy maintains −7.671 eV. This indicates that the initial adsorption of Na$_{ads}$ on the surface does not hinder the subsequent Na$_{inter}$ intercalation. However, intercalating Na$_{inter}$ significantly weakens the interaction between Na$_{ads}$ and dG, with the binding energy between the Na$_{ads}$-dG decreasing to −5.985 eV and the Na$_{ads}$-C distance increasing to 9.12 Å. This suggests that Na$_{inter}$ intercalation weakens the existing Na$_{ads}$-dG interactions.

A charge density difference analysis reveals significant charge transfer between surface Na$_{ads}$ and dG, with the transferred charge delocalized around the Stone Wales defect sites (Figure 4c), facilitating the formation of Na$_{ads}$-C interactions. When Na is intercalated between the interlayers, there is substantial charge transfer from Na$_{inter}$ to dG, which reduces the surface electron density of dG (Figure 4c, indicated by cyan), rendering the dG surface more positively charged. This increase in

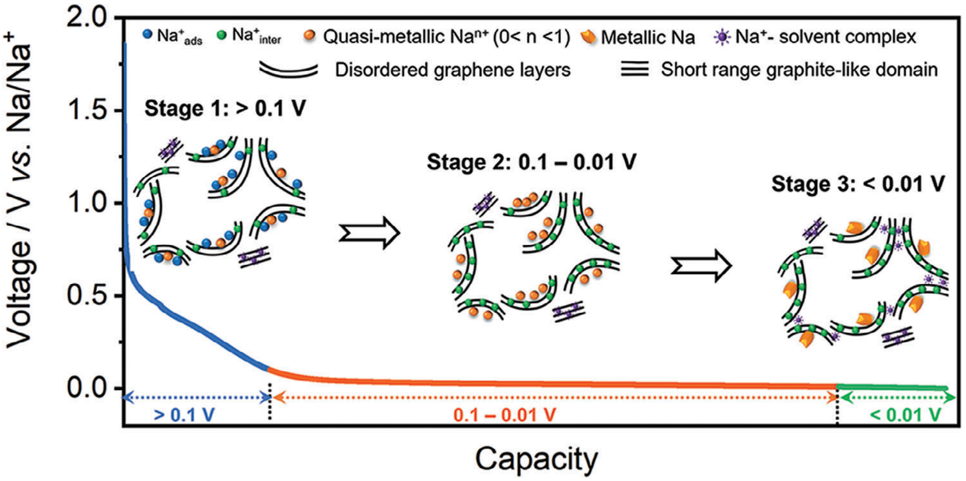

Figure 5. Schematic illustration of the Na ion storage mechanism in the HC.

positive charge enhances Coulomb repulsion interaction between Na_{ads} and dG, significantly weakening Na_{ads}-C interactions. As these interactions rely on electron density donation from Na_{ads} to the graphene matrix, their weakening implies that less valence electron density is transferred from Na_{ads} to graphene. This allows Na_{ads} to retain more of its valence electron density, driving it toward a quasi-metallic state.[11d] The density of states (DOS) spectra of Na_{ads} on the surface of Na_{ads}-dG, shown in Figure 4d, feature broadened partial density of states (PDOS) of the Na *s* and *p* orbitals, indicating hybridization of Na orbitals with C orbitals promoted by electron transfer from the electropositive Na_{ads} to defect sites. However, with the Na intercalation as illustrated in the Na_{ads}-dG-Na_{inter} model, sharp PDOS of the Na_{ads} *s* and *p* orbitals are observed, with the total DOS significantly shifted to the right (a higher $E-E_f$), confirming that less charge is transferred between Na_{ads} and dG.

Therefore, the Na ion intercalation between the dG layers drives the transition of the Na_{ads} from ionic to quasi-/metallic as schematically illustrated in Figure 4e. In the sloping region, the Na ion intercalation does not occur intensively, which is insufficient to induce substantial charge transfer with the dG, resulting in only a small portion of ionic Na transitioning to a quasi-metallic state. This observation aligns with the detection of a very weak C2 signal in this voltage region. Upon further discharge into the plateau region, intensive charge transfer occurs between the intercalated Na_{inter} and the dG, leading to much weaker Na_{ads}-C interactions and facilitating the formation of quasi-metallic Na clusters. Ultimately, the continued aggregation and growth of these quasi-metallic Na clusters culminate in the formation of metallic Na, confirmed by the in situ synchrotron XRD characterization.

3. Discussion

The above characterizations reveal that the Na ion storage in HC involves multiple processes, including Na ion intercalation, Na^+-solvent co-intercalation, and a transition of sodium species from ionic to quasi-/metallic. The EPR analysis of component C1 provides direct evidence of the Na ion intercalation process in HC, a detail that is challenging through XRD and in situ Raman data (Figure 1e,f). The Na ion intercalation process is illustrated in **Figure 5**. Initiated in the sloping region (stage 1), the Na ion intercalation process becomes more efficient in the subsequent plateau region, particularly in the voltage range between 0.1 and 0.01 V (stage 2). This is implied by a significant increase in the signal intensity of C1, indicating an increasing concentration of intercalated Na ions in the HC.

The EPR signal of C2, associated with sub-/nano-scale Na species exhibiting quasi-/metallic electronic properties, is observed throughout the reaction process. In situ synchrotron XRD and ^{23}Na MAS NMR characterizations further reveal that metallic Na is detected exclusively within the voltage range below 0.0148 V (stage 3), whereas quasi-metallic Na species are identified above this voltage range (stage 1 and 2). These findings indicate that the type of Na species stored in the HC varies with the SOD. This sequential transition of Na species—from ionic to quasi-metallic to metallic—during discharge provides crucial new insights into the dynamic electrochemical mechanisms in HC.

Additionally, the detection of C3 reveals that Na^+-solvent co-intercalation occurs in HC, a process that is difficult to detect using traditional characterization methods. From previous work, the co-interaction of Na^+-solvent complexes has been identified as the primary mechanism that enables graphite to be an electrochemically active electrode for storing Na ions in ether-based electrolytes. However, this process typically occurs in the high voltage range.[28a,b] Therefore, in the sloping region, the Na^+-solvent co-intercalation is expected to be present in the short range HC domains that exhibit graphite-like order (stage 1), where the intercalation between the solvent molecules and the graphene layer helps to stabilize the distribution of Na ions in these regions. However, this process is limited at this stage, as C3 exhibits a very weak signal intensity, indicating that only a small percentage of Na ions are stored through this mechanism. The co-intercalation process becomes more prominent in the low voltage region below 0.01 V (stage 3). Notably, C3 was also observed in the HC discharged in an ester-based electrolyte (Figure S13, Supporting Information). Na^+-solvent co-intercalation is thus most likely to occur in specific areas that provide a niche environment with weak interlayer interactions, which are unable to fully desolvate the Na ions from their solvated state. These regions are likely to be certain pores between the carbon domains that are accessible to the electrolyte rather than the closed pores in the HC.

Based on the above analysis, it can be seen that the microstructural properties of the HC play a crucial role in determining Na ion storage pathways. Optimizing these properties is essential for enhancing Na ion storage performance, which can be effectively accomplished through a carefully designed thermal treatment process. Furthermore, introducing Stone-Wales defects offers an additional strategy for increasing Na ion storage capacity. These defects promote surface Na ion adsorption and facilitate Na ion intercalation, providing an avenue to boost HC capacity through defect engineering. However, the progressive metallic transition of Na ions at defect sites, particularly the formation of metallic Na, poses a potential safety concern. Thus, precise control over defect concentration is critical to balance the enhanced Na ion storage capacity with mitigating metallic Na formation. Furthermore, Na^+-solvent co-intercalation emerges as a promising mechanism for further increasing Na ion storage in HC.

4. Conclusion

High-resolution CW and pulse EPR spectroscopy, combined with in situ experimental and theoretical investigations have enabled an in depth understanding of Na ion storage processes in the HC anode at an electronic level. Three distinct electrochemical processes are identified, including: Na ion intercalation between the graphene layers in both sloping and plateau regions, with a predominant contribution in the plateau region. In addition to this, Na^+-solvent co-intercalation occurs in carbon domains with graphite-like order or in certain pores between the carbon domains, with the occurrence depending on the state of discharge. Furthermore, Na ions are adsorbed on Stone-Wales defect sites on the surface of graphene layers in the sloping region. These Na ions simultaneously evolve into quasi-metallic Na, which progressively undergo metallization within the plateau region, ultimately transitioning to metallic Na in the low voltage region below 0.01 V. This transformation is driven by charge redistribution between intercalated Na ions and graphene layers, facilitated by continuous Na ion intercalation. This work demonstrates the unique capabilities of EPR spectroscopy in probing the charge storage mechanisms of battery electrode materials.

5. Experimental Section

Sample Preparation: The hard carbon (HC) studied in this work was obtained from Thermo Fisher Scientific.

Structural Characterizations: The microstructure of the HC was characterized using a scanning transmission electron microscope (TEM, Hitachi HF5000), X-ray diffraction (XRD) with Cu Kα radiation source (Bruker D8) with an X-ray wavelength is 1.54184 Å, and Raman spectroscopy with a 514 nm incident laser (Renishaw).

Electrochemical Characterizations: To prepare the HC electrode, HC powder was mixed with polyvinylidene fluoride (PVDF) in a weight ratio of 95:5 in N-Methyl-2-pyrrolidone (NMP) solution to form a uniform slurry. Then, the slurry was uniformly coated onto Cu foil and dried at 120 °C for 24 h in a vacuum oven. The as-prepared electrode was cut into pieces with a diameter of 10 mm. The electrochemical performance was evaluated in three-electrode cells with the HC electrode as the working electrode; Na metal as the counter electrode and reference electrode, a glass fiber separator, and 1 м $NaPF_6$ in diglyme solvent as the electrolyte. The cells were assembled in a glove box under an Ar atmosphere with $O_2 < 0.1$ ppm and $H_2O < 0.1$ ppm. Galvanostatic charge/discharge tests were conducted on a Biologic VMP-3 electrochemical workstation between 0 and 3.0 V at a current density of 10 mA g^{-1} at room temperature.

Sample Preparation for Ex Situ EPR Characterizations: To prepare the samples for ex situ EPR characterization, the cells were initially discharged to various SOD, specifically 0.5, 0.3, 0.2, 0.1, 0.01, 0 V. Subsequently, the cells were disassembled in a glovebox, the resulting GC electrodes were washed with diglyme solvent and then dried under vacuum in a vacuum transfer chamber for 12 h. Finally, the sodiated HC electrodes were sealed in Ar-filled thin-wall quartz tubes (3 mm outside diameter). For the temperature-dependent continuous-wave (CW) EPR characterizations, the quartz tubes were evacuated to a pressure of 1×10^{-4} Pa, and then the tubes were sealed using a blow torch.

X-Band and Q-Band CW and Pulse EPR Spectroscopy Characterizations: X-band (ca. 9.8658 GHz) CW EPR spectra were recorded on a Bruker Elexsys E500 spectrometer equipped with a Bruker Dual Mode resonator and He cooling (Bruker waveguide Cryogen-free system with recirculator, WVGD SYS 5K F70H wRCRC 2). The magnetic field was calibrated with 2,2-diphenyl-1-picrylhydrazyl ($g = 2.0036$), and measurements were carried out in the temperature range of 5–295K.

Q-band and all pulse data were acquired on a Bruker ElexE580 spectrometer equipped with a 1 kW TWT Amplifier at X-band (Model 117X, Applied Systems Engineering, Inc) and a 150 W TWT Amplifier at Q-band (Model 187Ka, Applied Systems Engineering, Inc), and a cryogen-free variable temperature cryostat (No. 3679A, Cryogenics, Inc). Q-band measurement used a Bruker ER5106QT-2 probehead (allowing 3 mm tube access).

The free induction decay (FID) detected field-swept spectra were acquired by integration of the signal (FID) from a single microwave pulse of length 500 ns. The echo-detected field-swept spectra were acquired using the sequence of $\pi/2$-τ-π-τ-echo, with $t_{\pi/2} = 100$ ns, $\tau = 480$ ns, $t_{\pi} = 200$ ns. For both techniques, the derivative of the recorded absorption spectrum was calculated numerically with MatLab using a 2nd order polynomial fitted ±5 points either side of the intensity point being processed.

X-band Hyperfine sublevel correlation (HYSCORE) experiments were carried out at 15 K employing the pulse sequence $\pi/2 - \tau - \pi/2 - t_1 - \pi - t_2 - \pi/2 - \tau$ -echo, using mw pulses of lengths $t_{\pi/2} = 16$ ns, starting times $t_1 = t_2 = 32$ ns, $\tau = 134$ ns (matrix ^1H blind-spot), repetition time 1 ms, and time increments of $\Delta t = 16$ ns (data matrix 160 × 160).[26,30] A four-step phase cycle was used to remove unwanted echoes. The observer position was the echo maximum at the center of the spectrum. The HYSCORE data were processed with MATLAB; time traces were baseline corrected with an exponential, apodized with a Gaussian window, and zero filled. After a 2D Fourier transformation absolute-value spectra were calculated.

Ex Situ ^{23}Na MAS NMR Characterization: Ex situ ^{23}Na MAS NMR characterization was conducted on a Bruker Avance III 300 MHz spectrometer. First, the HC electrodes were discharged to the target SODs at a current density of 10 mA g^{-1} in three-electrode cells. Then, the electrodes were collected, washed with DMC, and dried in a vacuum chamber attached to the glovebox. Before characterization, the HC was scraped from the Cu foil and sealed into zirconia rotors in a glovebox.

In Situ Raman Characterization: In situ Raman characterization was conducted with a Raman spectroscope (Renishaw) with a 514 nm incident laser. A customized (MTI Corporation) in situ setup with a hole on the cathode side was used for the experiment. To prepare the HC electrode for the in situ Raman characterization, the HC was mixed with NMP in a weight ratio of 9:1 to form a uniform slurry. The slurry was coated onto a titanium mesh and dried at 120 °C for 12 h in a vacuum oven. The in situ cell was assembled using the as-prepared electrodes as the cathode, sodium metal as the anode, and glass fiber soaked with 1 м $NaPF_6$ in diglyme solvent as the electrolyte. The hole was sealed using a quartz window. The cell was discharged using a Biologic VMP-3 electrochemical workstation at a current density of 10 mA g^{-1}. Raman spectra were collected in the spectra range 1000–2000 cm^{-1}. A 50× objective was used to focus the laser light onto the electrode surface to collect the Raman signal. The laser power was set to 5 mW, and the spectrum acquisition was finished in 30 s.

In Situ Synchrotron X-ray Diffraction Characterization: In situ synchrotron X-ray diffraction (XRD) patterns were measured at the Powder Diffraction Beamline, Australian Synchrotron. An X-ray wavelength of 0.6877 Å was employed for the in situ characterization. The in situ cells were assembled using the HC as a working electrode, glass fiber separator, and sodium metal as a counter electrode in a commercial 2032-type coin cell with a hole punched through the casing (both sides) to allow X-rays to transmit. The holes were covered by the Kapton tape (practically X-ray transparent) to avoid exposing the electrode to air. The cells were galvanostatic discharged/charged during the tests at a current density of 10 mA g^{-1} in a Neware battery test system.

Density Functional Theory Calculations: The calculations were performed within the framework of density functional theory (DFT) using the Vienna *Ab-initio* Simulation Package (VASP) code, employing the projector augmented wave method with the Perdew–Burke–Ernzerhof (PBE) exchange-correlation functional.[31] Two structural models of pristine graphene and Stone-Wale defect-containing graphene were considered. In the models, there are 64 C and 2 Na_{ads} in the models Na_{ads}-pG, Na_{ads}-dG, and Na_{ads}-dG-Na_{inter}, with 2 Na_{inter} in Na_{ads}-dG-Na_{inter}. Two and four electrons were removed from Na_{ads}-pG, Na_{ads}-dG and Na_{ads}-dG-Na_{inter}, respectively. The Van der Waals (vdW) interactions were considered using a modified version of the vdW-DF, denoted as "optB86b-vdW".[32] The projector augmented wave potentials were used with an energy cutoff of 600 eV.[33] The lattice constraints for graphene are 9.86 Å × 9.86 Å, with a vacuum layer larger than 20 Å perpendicular to the surface plane. A 4 × 4 × 1 Monkhorst-pack *k*-mesh scheme was used for geometry optimization, ensuring energy convergence of 1.0×10^{-4} meV $atom^{-1}$ during the self-consistent field calculations. The convergence criteria for the atomic forces was set to 0.01 eV $Å^{-1}$. The *k*-meshes were doubled for single-point calculation. The adsorption energies E_{ad} were calculated according to the equation:

$$E_{ad} = E_{total} - E_{ion} - E_{slab} \tag{1}$$

where E_{total}, E_{ion}, and E_{slab} are the energies of the adsorption system, adsorbed ion, and graphene slab, respectively. A more negative adsorption energy indicates a more stable adsorption configuration. Additionally, the charge density differences, and density of state (DOS) were extracted from the static calculation. The charge density difference was visualized by VESTA.

Supporting Information

Supporting Information is available from the Wiley Online Library or from the author.

Acknowledgements

This work was funded by the Australian Research Council through grants DP200102573, FT220100666, and LE230100048. The authors gratefully acknowledge the support provided by the Centre of Microscopy and Microanalysis (CMM) and the EPR facility at the The University of Queensland. The authors also thank the support received from the Powder Diffraction beamline at the Australian Synchrotron, part of ANSTO. The authors express their gratitude to Prof. Xiu Song (George) Zhao from The University of Queensland (now at Qingdao University) for his generous support in facilitating this work.

Open access publishing facilitated by The University of Queensland, as part of the Wiley - The University of Queensland agreement via the Council of Australian University Librarians.

Conflict of Interest

The authors declare no conflict of interest.

Data Availability Statement

The data that support the findings of this study are available in the supplementary material of this article.

Keywords

charge storage mechanism, electron paramagnetic resonance, hard carbon, radicals, sodium-ion batteries

Received: December 9, 2024
Revised: January 28, 2025
Published online:

---

[1] D. Larcher, J. M. Tarascon, *Nat. Chem.* **2015**, *7*, 19.
[2] a) R. Usiskin, Y. X. Lu, J. Popovic, M. Law, P. Balaya, Y. S. Hu, J. Maier, *Nat. Rev. Mater.* **2021**, *6*, 1020; b) J. Zhang, Y. Wang, Q. Xia, X. Li, B. Liu, T. Hu, M. Tebyetekerwa, S. Hu, R. Knibbe, S. Chou, *Angew. Chem., Int. Ed.* **2024**, *63*, 202318822; c) E. R. Cooper, M. Li, I. Gentle, Q. Xia, R. Knibbe, *Angew. Chem., Int. Ed.* **2023**, *62*, 202309247.
[3] a) J. M. Tarascon, *Joule* **2020**, *4*, 1616; b) Q. B. Xia, Y. R. Liang, E. R. Cooper, C. L. Ko, Z. Hu, W. J. Li, S. L. Chou, R. Knibbe, *Adv. Energy Mater.* **2024**, *14*, 2400929; c) Q. Xia, Y. Huang, J. Xiao, L. Wang, Z. Lin, W. Li, H. Liu, Q. Gu, H. K. Liu, S. L. Chou, *Angew. Chem., Int. Ed.* **2019**, *58*, 4022; d) Q. Xia, Z. Lin, W. Lai, Y. Wang, C. Ma, Z. Yan, Q. Gu, W. Wei, J. Z. Wang, Z. Zhang, H. K. Liu, S. X. Dou, S. L. Chou, *Angew. Chem., Int. Ed.* **2019**, *58*, 14125; e) Q. B. Xia, Y. R. Liang, Z. H. Lin, S. W. Wang, W. H. Lai, D. Yuan, Y. H. Dou, Q. F. Gu, J. Z. Wang, H. K. Liu, S. X. Dou, S. M. Fang, S. L. Chou, *Adv. Energy Mater.* **2020**, *10*, 2001033; f) L.-Y. Kong, J.-Y. Li, H.-X. Liu, Y.-F. Zhu, J. Wang, Y. Liu, X.-Y. Zhang, H.-Y. Hu, H. Dong, Z.-C. Jian, C. Cheng, S. Chen, L. Zhang, J.-Z. Wang, S. Chou, Y. Xiao, *J. Am. Chem. Soc.* **2024**, *146*, 32317; g) E. Wang, J. Wan, Y.-J. Guo, Q. Zhang, W.-H. He, C.-H. Zhang, W.-P. Chen, H.-J. Yan, D.-J. Xue, T. Fang, F. Wang, R. Wen, S. Xin, Y.-X. Yin, Y.-G. Guo, *Angew. Chem., Int. Ed.* **2023**, *62*, 202216354; h) Q. Xia, H. Liu, X. S. Zhao, *J. Mater. Chem. A* **2022**, *10*, 3889.
[4] N. Yabuuchi, K. Kubota, M. Dahbi, S. Komaba, *Chem. Rev.* **2014**, *114*, 11636.
[5] J. Y. Hwang, S. T. Myung, Y. K. Sun, *Chem. Soc. Rev.* **2017**, *46*, 3529.
[6] a) N. Sun, J. Qiu, B. Xu, *Adv. Energy Mater.* **2022**, *12*, 2200715; b) H. S. Hou, X. Q. Qiu, W. F. Wei, Y. Zhang, X. B. Ji, *Adv. Energy Mater.* **2017**, *7*, 1602898; c) M. Thompson, Q. B. Xia, Z. Hu, X. S. Zhao, *Mater. Adv.* **2021**, *2*, 5881.
[7] a) D. A. Stevens, J. R. Dahn, *J. Electrochem. Soc.* **2000**, *147*, 4428; b) D. A. Stevens, J. R. Dahn, *J. Electrochem. Soc.* **2001**, *148*, A803.
[8] Y. Cao, L. Xiao, M. L. Sushko, W. Wang, B. Schwenzer, J. Xiao, Z. Nie, L. V. Saraf, Z. Yang, J. Liu, *Nano Lett.* **2012**, *12*, 3783.
[9] a) C. Bommier, T. W. Surta, M. Dolgos, X. Ji, *Nano Lett.* **2015**, *15*, 5888; b) Y. Morikawa, S. Nishimura, R. Hashimoto, M. Ohnuma, A. Yamada, *Adv. Energy Mater.* **2020**, *10*, 1903176; c) S. Alvin, H. S. Cahyadi, J. Hwang, W. Chang, S. K. Kwak, J. Kim, *Adv. Energy Mater.* **2020**, *10*, 2000283; d) S. Qiu, L. F. Xiao, M. L. Sushko, K. S. Han, Y. Y. Shao, M. Y. Yan, X. M. Liang, L. Q. Mai, J. W. Feng, Y. L. Cao, X. P. Ai, H. X. Yang, J. Liu, *Adv. Energy Mater.* **2017**, *7*, 1700403; e) Z. Li, C. Bommier, Z. S. Chong, Z. Jian, T. W. Surta, X. Wang, Z. Xing, J. C. Neuefeind, W. F. Stickle, M. Dolgos, P. A. Greaney, X. Ji, *Adv. Energy Mater.* **2017**, *7*, 1602894; f) X. Y. Chen, J. Y. Tian, P. Li, Y. L. Fang, Y. J. Fang, X. M. Liang, J. W. Feng, J. Dong, X. P. Ai, H. X. Yang, Y. L. Cao, *Adv. Energy Mater.* **2022**, *12*, 2200886.
[10] a) X. Yin, Z. Lu, J. Wang, X. Feng, S. Roy, X. Liu, Y. Yang, Y. Zhao, J. Zhang, *Adv. Mater.* **2022**, *34*, 2109282; b) M. E. Lee, S. M. Lee, J. Choi, D. Jang, S. Lee, H. J. Jin, Y. S. Yun, *Small* **2020**, *16*, 2001053.

[11] a) F. Xie, Z. Xu, A. C. S. Jensen, H. Au, Y. Lu, V. Araullo-Peters, A. J. Drew, Y.-S. Hu, M.-M. Titirici, *Adv. Funct. Mater.* **2019**, *29*, 1901072; b) B. Zhang, C. M. Ghimbeu, C. Laberty, C. Vix-Guterl, J.-M. Tarascon, *Adv. Energy Mater.* **2016**, *6*, 1501588; c) H. Kim, J. C. Hyun, D. H. Kim, J. H. Kwak, J. B. Lee, J. H. Moon, J. Choi, H. D. Lim, S. J. Yang, H. M. Jin, D. J. Ahn, K. Kang, H. J. Jin, H. K. Lim, Y. S. Yun, *Adv. Mater.* **2023**, *35*, 2209128; d) Y. Li, A. Vasileiadis, Q. Zhou, Y. Lu, Q. Meng, Y. Li, P. Ombrini, J. Zhao, Z. Chen, Y. Niu, X. Qi, F. Xie, R. van der Jagt, S. Ganapathy, M.-M. Titirici, H. Li, L. Chen, M. Wagemaker, Y.-S. Hu, *Nat. Energy* **2024**, *9*, 134.

[12] a) M. A. Reddy, M. Helen, A. Groß, M. Fichtner, H. Euchner, *ACS Energy Lett.* **2018**, *3*, 2851; b) P. Bai, Y. He, X. Zou, X. Zhao, P. Xiong, Y. Xu, *Adv. Energy Mater.* **2018**, *8*, 1703217.

[13] a) J. M. Stratford, P. K. Allan, O. Pecher, P. A. Chater, C. P. Grey, *Chem. Commun.* **2016**, *52*, 12430; b) H. Au, H. Alptekin, A. C. S. Jensen, E. Olsson, C. A. O'Keefe, T. Smith, M. Crespo-Ribadeneyra, T. F. Headen, C. P. Grey, Q. Cai, A. J. Drew, M. M. Titirici, *Energy Environ. Sci.* **2020**, *13*, 3469.

[14] a) X. Li, L. Zhang, H. Liu, Q. Li, Y. Hou, *Adv. Energy Mater.* **2023**, *13*, 2300927; b) Q. Li, J. Zhang, L. Zhong, F. Geng, Y. Tao, C. Geng, S. Li, B. Hu, Q.-H. Yang, *Adv. Energy Mater.* **2022**, *12*, 2201734.

[15] H. Nguyen, R. J. Clément, *ACS Energy Lett.* **2020**, *5*, 3848.

[16] D. Saurel, B. Orayech, B. W. Xiao, D. Carriazo, X. L. Li, T. Rojo, *Adv. Energy Mater.* **2018**, *8*, 1703268.

[17] H. Fujimoto, *Carbon* **2003**, *41*, 1585.

[18] a) P. J. F. Harris, *Int. Mater. Rev.* **1997**, *42*, 206; b) P. J. F. Harris, *Philos. Mag.* **2004**, *84*, 3159; c) G. M. Jenkins, K. Kawamura, *Nature* **1971**, *231*, 175.

[19] M. S. Dresselhaus, G. Dresselhaus, R. Saito, A. Jorio, *Phys. Rep.* **2005**, *409*, 47.

[20] a) H. Yadegari, M. A. Koronfel, K. Wang, D. B. Thornton, I. E. L. Stephens, C. Molteni, P. D. Haynes, M. P. Ryan, *ACS Energy Lett.* **2021**, *6*, 1633; b) A. P. Cohn, K. Share, R. Carter, L. Oakes, C. L. Pint, *Nano Lett.* **2016**, *16*, 543.

[21] J. Sun, M. Sadd, P. Edenborg, H. Gronbeck, P. H. Thiesen, Z. Xia, V. Quintano, R. Qiu, A. Matic, V. Palermo, *Sci. Adv.* **2021**, *7*, eabf0812.

[22] J. Wang, H. Wang, R. Zhao, Y. Wei, F. Kang, D. Zhai, *Nano Lett.* **2022**, *22*, 6359.

[23] a) Y.-P. Wu, C.-R. Wan, C.-Y. Jiang, S.-B. Fang, Y.-Y. Jiang, *Carbon* **1999**, *37*, 1901; b) E. Zhecheva, R. Stoyanova, J. M. Jiménez-Mateos, R. Alcántara, P. Lavela, J. L. Tirado, *Carbon* **2002**, *40*, 2301; c) Y. Yafet, in *Solid State Physics*, *14*, (Eds.: F. Seitz, D. Turnbull), Academic Press, New York, USA **1963**, pp. 1–98.

[24] S. Blundell, *Magnetism in Condensed Matter*, Oxford University Press, United States, **2001**.

[25] a) M. S. Dresselhaus, G. Dresselhaus, *Adv. Phys.* **2002**, *51*, 1; b) M. L. Tiago, J. E. Northrup, S. G. Louie, *Phys. Rev. B* **2003**, *67*, 115212.

[26] A. Schweiger, G. Jeschke, *Principles of Pulse Electron Paramagnetic Resonance*, Oxford University Press, Oxford, UK **2001**.

[27] a) Z. Wang, X. Feng, Y. Bai, H. Yang, R. Dong, X. Wang, H. Xu, Q. Wang, H. Li, H. Gao, C. Wu, *Adv. Energy Mater.* **2021**, *11*, 2003854; b) J. M. Stratford, A. K. Kleppe, D. S. Keeble, P. A. Chater, S. S. Meysami, C. J. Wright, J. Barker, M. M. Titirici, P. K. Allan, C. P. Grey, *J. Am. Chem. Soc.* **2021**, *143*, 14274; c) Q. Li, X. Liu, Y. Tao, J. Huang, J. Zhang, C. Yang, Y. Zhang, S. Zhang, Y. Jia, Q. Lin, Y. Xiang, J. Cheng, W. Lv, F. Kang, Y. Yang, Q. H. Yang, *Natl. Sci. Rev.* **2022**, *9*, nwac084.

[28] a) B. Jache, P. Adelhelm, *Angew. Chem., Int. Ed.* **2014**, *53*, 10169; b) H. Kim, J. Hong, G. Yoon, H. Kim, K.-Y. Park, M.-S. Park, W.-S. Yoon, K. Kang, *Energy Environ. Sci.* **2015**, *8*, 2963; c) R. Dong, L. Zheng, Y. Bai, Q. Ni, Y. Li, F. Wu, H. Ren, C. Wu, *Adv. Mater.* **2021**, *33*, 2008810.

[29] a) A. Gomez-Martin, J. Martinez-Fernandez, M. Ruttert, M. Winter, T. Placke, J. Ramirez-Rico, *Chem. Mater.* **2019**, *31*, 7288; b) K. Kubota, S. Shimadzu, N. Yabuuchi, S. Tominaka, S. Shiraishi, M. Abreu-Sepulveda, A. Manivannan, K. Gotoh, M. Fukunishi, M. Dahbi, S. Komaba, *Chem. Mater.* **2020**, *32*, 2961.

[30] P. Höfer, A. Grupp, H. Nebenführ, M. Mehring, *Chem. Phys. Lett.* **1986**, *132*, 279.

[31] a) G. Kresse, J. Furthmüller, *Phys. Rev. B* **1996**, *54*, 11169; b) P. E. Blöchl, *Phys. Rev. B* **1994**, *50*, 17953; c) J. P. Perdew, K. Burke, M. Ernzerhof, *Phys. Rev. Lett.* **1996**, *77*, 3865.

[32] a) J. Klimeš, D. R. Bowler, A. Michaelides, *J. Phys.: Condens. Matter* **2010**, *22*, 022201; b) J. Klimeš, D. R. Bowler, A. Michaelides, *Phys. Rev. B* **2011**, *83*, 195131.

[33] G. Kresse, D. Joubert, *Phys. Rev. B* **1999**, *59*, 1758.